Case Studies in Thermal Engineering 38 (2022) 102364

Contents lists available at ScienceDirect

Case Studies in Thermal Engineering

journal homepage: www.elsevier.com/locate/csite

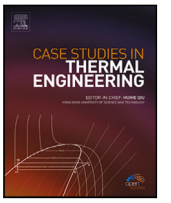

Thermal–hydraulic separators unveiled

Marzio Piller *, Luca Toneatti

Dipartimento di Ingegneria e Architettura, Università degli Studi di Trieste, via A. Valerio 10, 34127 Trieste, Italy

ARTICLE INFO

Keywords:
Hydraulic separator
Thermal dispatcher
Block model
Mesh strainer
Computational fluid dynamics

ABSTRACT

A key issue in the design of heating/cooling networks consists in attaining the hydraulic independence of the connected circuits while simultaneously providing the required flow rate of thermal fluid at the design temperature under different operation loads. In this respect, thermal–hydraulic separators offer a valid alternative over other devices used for the same service (as, e.g., heat exchangers, accumulation tanks or double-tee junctions), providing the opportunity to integrate the functions of de-gassing and of removal of solid debris in a single piece of equipment.

The present numerical investigation improves the characterization and modelling of these devices. The major outcome of the proposed research is the improvement of the *base* model widely-used in the design of thermal–hydraulic networks encompassing thermal–hydraulic separators. The proposed model accounts for the turbulent mixing within the device. Furthermore, we propose an original network representation of thermal–hydraulic separators, which supports the physical intuition about their internal flow patterns and can be integrated in thermal network solvers used for plant design and optimization. To the authors' best knowledge, this is the first numerical investigation accounting for the impact of the internal mesh strainer on the behaviour of the device.

1. Introduction

Hydraulic networks used for heating and cooling purposes transfer thermal power from the heat sources/sinks to the consuming systems. A *primary* circuit (PC) is connected with the heat source/sink, while one or more *secondary* piping systems (SC) supply the thermal fluid (mostly water or anti-freeze solution) to different consuming systems. Nowadays, various options exist to thermally connect the PCs with the SCs: the connection strategy must meet some requirements which favour the ongoing, efficient and safe operation of the plant. The designed amount of fluid must be supplied to all the consumer circuits both under full and under partial load operation. Heat sources should operate within their optimal range and must be protected from overheating upon the switching off of most or of all heating terminals. The clogging of the flow passages caused by the accumulation of solid debris must be prevented. The connection devices should provide a negligible contribution to the thermal inertia of the whole system. Furthermore, one of the most significant requirements is that the connection strategy must ensure the mutual hydraulic separation of the served circuits. Thermal–hydraulic separators (THS) are hydraulic components that, if properly designed, do satisfy the aforementioned requirements. Their robust construction, lacking of moving parts, the wide flow sections that are not prone to be clogged by sediments and the opportunity to combine in a single piece of equipment the functions of hydraulic separation, thermal dispatching, de-gassing and removal of solid debris do justify the practical interest towards this class of devices. The present investigation shows that the considered family of geometrically-similar THSs induces a moderate prevalence on the connected circuits under a wide

* Corresponding author.
E-mail addresses: piller@units.it (M. Piller), luca.toneatti@dia.units.it (L. Toneatti).

https://doi.org/10.1016/j.csite.2022.102364
Received 9 March 2022; Received in revised form 21 July 2022; Accepted 6 August 2022
Available online 12 August 2022

Nomenclature

Abbreviations

BIP, PIP, POP, BOP	Inflow/outflow openings, according to Fig. 1
CCCP-DH	Central circulating pumps
DVSP-DH	Distributed variable speed pumps
HC	Heat consumer
HS	Heat source
LIC	line-integral-convolution
MTS	Mesh-type strainer
ODE	Ordinary differential equation
PC	Primary circuit
SC	Secondary circuit
THS	Thermal–hydraulic separator

Symbols

$\boldsymbol{n}$	Unit vector normal to a surface
ΔT [K]	Temperature decay throughout the heat-consuming system
ΔP_{tot} [Pa]	Difference in P_t between two open sections of the THS, located at a distance of $1\,d$ from the barrel's case
$\dot{m}$ [kg s^{-1}]	Mass-flow rate
τ_w [Pa]	Wall shear stress
c_1, c_2, a, b, d, h, H, L, s, S [mm]	characteristic lengths (see Fig. 1 and Table 2)
c_p [J kg^{-1} K^{-1}]	Specific heat capacity of water
k [W m^{-1} K^{-1}]	Thermal conductivity
P_t [Pa]	Modified total pressure
T_1, T_2, T_3, T_4 [K]	bulk fluid temperatures at BIP, PIP, POP, BOP
u_τ [m s^{-1}]	Friction velocity, $u_\tau = \sqrt{\frac{\tau_w}{\rho}}$
w [m s^{-1}]	Vertical velocity component
y^+	Wall normal distance, in wall units: $y^+ = y\,u_\tau/\nu$.
$\mathbf{g}$ [m s^{-2}]	Gravitational acceleration
$\mathbf{u}$ [m s^{-1}]	Velocity
$\mathbf{x}$ [m]	Position
P [Pa]	Gauge pressure, Eq. (3)
p [Pa]	Static pressure
Pe	Peclét number, Eq. (11)
Pr	Prandtl number, Eq. (11)
Re	Reynolds number, Eq. (11)
Ri	Richardson number, Eq. (11)
T [K]	Temperature
t [s]	Time
U [m s^{-1}]	Mean inflow velocity through the BIP

Greek symbols

α_0 [K^{-1}]	Coefficient of volume expansion
β	Relative flow rate of the bypass stream (Section 2.1 and Table 3)
γ	Ratio of mass-flow rates of secondary by primary circuit
μ [kg m^{-1} s^{-1}]	Dynamic viscosity of water
ν	Kinematic viscosity
Π^*	Non-dimensional, gauge pressure, Eq. (7)
ρ [kg m^{-3}]	Density

range of operation conditions, attaining their hydraulic independence. Furthermore, it is verified that THSs supply the necessary amount of fluid to the secondary circuits, with a temperature that is nearly independent of the heat consumption load, provided the primary flow rate exceeds the secondary flow rate.

ϑ	Non-dimensional temperature, Eq. (7)
ξ_t	Head loss coefficient (Eq. (14))
Subscripts	
PC	Primary (or heat supply) circuit
SC	Secondary (or heat consuming) circuit
0	Reference (pressure, temperature) conditions
Superscripts	
$*$	Non-dimensional quantities, Eq. (7)

THSs are often used as thermo-hydraulic dispatchers in heat supply systems: the hot/cold water supplied to the THS by the heating/cooling plant is transferred to one or more heat exchange networks. Yan et al. [1] compare district heating systems with *distributed variable speed pumps* (DVSP-DH) and with a conventional *central circulating pump* (CCCP-DH), respectively. In DVSP-DH systems the primary and secondary circuits are linked by a hydraulic connector pipe with low hydraulic resistance, thereby reducing significantly the hydraulic interaction of the heat-supply and heat-consuming networks. In DVSP-DH networks, a pump is installed at each substation of the secondary network, making unnecessary the central circulating pump and the control valves, used to distribute the flow among substations in CCCP-DH systems. This, in turn, allows for significant energy savings, as the power loss related to throttling is avoided. Yan et al. [1] report that substituting a CCCP-DH system with a DVSP-DH system in a district heating plant in Kuerle, China, resulted in a reduction of pumping power from 238 kW to 194 kW and in about 30% energy saving under changing flow rates of one or several consumers.

Yavorovsky et al. [2] investigate by numerical simulation the flow and temperature distribution inside two different types of THS, differing in the arrangement of the connecting pipes. The reported results provide evidence that, for the considered THS configurations, the temperature of the fluid supplied to the heat-consuming circuit is significantly independent either of the flow rate through the heat-supply network or of the ratio γ between the flow rates of secondary to primary circuits. The temperature of the fluid returning to the heat-supply system is significantly independent of the flow rate through it, while it decreases approximately linearly with increasing γ, as predicted by the ideal operation model of the separator.

Yavorovsky et al. [3] propose a combined experimental and numerical investigation on a THS used to connect a boiler with two heating terminal units. It turns out that the secondary circuits are indeed hydraulically separated from each other: changing the flow rate through one of them does not significantly affect the supply/return temperatures and the heat rejection of the other.

Despite the wide application of THSs in decentralized heat supply systems [4] and in district-heating systems [2], the design of THSs is still predominantly based on empirical rules derived from experience, as the *three-diameters* rule or the *alternate connections method* [5].

Anisimova [4] investigates a THS with aligned manifolds, connected to four heating terminal units through a water distribution manifold. Four different operating modes are considered where some of the aforementioned heat consumers are partially or totally disconnected. The revealed pressure inhomogeneity within the THS is ascribed to gravitational stratification. The mixing taking place within the device causes a temperature drop of $2 \div 3$ K for the fluid supplied to the heat consumers: in this respect, the different findings of Yavorovsky et al. [2] and Anisimova [4] suggest that there is margin for further studies on the thermal behaviour of THSs: indeed, there is scarcity of theoretical and numerical studies concerning their operation and performance. Romanov and Yavorovsky [6] carry out a combined experimental and numerical investigation on a 8-manifold THS, considering different connection arrangements to an electric boiler and to two heating terminals. Toneatti et al. [7] propose a numerical investigation on the hydraulic and thermal performance of a family of geometrically-similar THSs, identifying the flow and temperature patterns existing within the device at different values of the flow-split ratio γ.

The aforementioned studies focus on THSs lacking of a mesh-type strainer (MTS), i.e., a perforated metal screen that increases the turbulence intensity within the device, thus allowing to efficiently remove air and solid debris (scale, rust and welding metals [8]). The resulting piece of equipment integrates the functions of hydraulic and thermal separation with the cleaning of the circulating fluid. In view of this favourable opportunity, the present numerical study proposes an original investigation about the hydraulic and thermal performance of a family of geometrically-similar THSs endowed with a mesh-type strainer.

Besides a detailed investigation on the internal flow and thermal pattern, we propose an original block-model encompassing four non-linear hydraulic resistances that can be integrated in network-based thermal–hydraulic solvers applied for plant design or optimization purposes, while also affording a conceptual framework for linking the pressure and temperature outcomes from the THS with its internal flow pattern: this source of information can be integrated in operation manuals of the device to convey the technical information required for plant-design purposes.

2. Materials and methods

2.1. Shape, size and operation of the considered hydraulic separator

The considered THS consists of a central body (*barrel*) with square cross section, mounting four lateral manifolds for the connection to the PC and SC. The large size of the body of hydraulic separators limits the vertical flow velocity within the device, thus

Table 1
Identification of the connection ports of the THS.

Index	Acronym	Flow direction			Inlet/outlet
1	BIP	PC	⟶	THS	Inlet
2	PIP	THS	⟶	SC	Outlet
3	POP	SC	⟶	THS	Inlet
4	BOP	THS	⟶	PC	Outlet

Table 2
Dimensions of the considered THSs in millimeters (see Fig. 1).

L	H	h	d	a	b	s	c_1	c_2	S
64	220	97	35	11.5	130	3	12	12	6

Table 3
Dimensionless fluid temperatures at the openings of the THS.

γ	ϑ_2	ϑ_3	ϑ_4
≤ 1	$\frac{\beta}{1-\beta}$	$1+\vartheta_2$	γ
>1	$\frac{\gamma}{1-\beta}-1$	$1+\vartheta_2$	γ

inducing a very modest head loss between the upper and lower connections, even under conditions of relatively intense recirculation of the primary or of the secondary flow (i.e., whenever γ deviates significantly from unity) [9]. This, in turn, implies that a hydraulic separator significantly limits the hydraulic interference between the connected piping systems. The THS may be equipped with a mesh strainer, which fosters the separation of the suspended air bubbles and solid debris. Upon being slowed down by the strained, the air bubbles rise to the top of the separator where they are vented out by an automatic air vent valve, while the solid impurities settle down and deposit at the bottom of the separator, whence they are discharged via a drain stopcock. THSs are usually embodied into a layer of thermal insulating material: therefore in the present work it is assumed that the case of the THSs is perfectly adiabatic. A schematic representation of the considered hydraulic separators is reported in Fig. 1. The naming and indexing convention of the connection manifolds are reported in Table 1: corresponding subscripts are used to denote the flow quantities at the inlet and outlet boundaries of the computational domain.

The considered THS resembles a commercially available piece of equipment: its characteristic dimensions are reported in Table 2. The geometric shape factors follow closely the 3-diameters design rule, except for the width L of the main body. The considered THS endows a mesh strainer consisting of a perforated steel plate with staggered rows of circular holes (see Fig. 1), featuring an open area ratio (void surface area by total surface area) $\epsilon \approx 39\%$.

Real-life applications of THSs mainly concern hydronic systems containing multiple circulators to be operated simultaneously (see Fig. 2). The circulators are said to be *hydraulically separated* from each other if the operation of any of them does not alter the flow rate or head of any other. One common application of hydraulic separators is the connection of multiple heat suppliers (e.g., boilers) with multiple heat sinks (e.g., radiators), as shown in Fig. 2: each independent primary or secondary circuit endows a circulating pump and a check valve and can be activated or stopped without significantly affecting the flow rate through the other branches of the network. According to [9], the head loss through the heat supply circuit, connecting the boilers, should be maintained very low by providing for a design flow velocity not larger than approximately 1 m/s.

The simplest, widely accepted operation model for THSs (*base* model) assumes that the turbulent and the molecular diffusion of heat are negligible and that no unpredicted bypass streams develop within the device. The internal flow distribution and the inflow/outflow mass-flow rates and temperatures are represented in Fig. 3, where β denotes the bypass secondary (for $\gamma < 1$) or primary (for $\gamma > 1$) flow rate. The aforementioned *base* operation model corresponds to $\beta = 0$: according to it, for $\gamma < 1$ part of the primary flow is recirculated and the temperature of the flow delivered to the SC equals the temperature of the flow supplied from the PC, while for $\gamma > 1$ part of the secondary flow is recirculated and the temperature of the fluid supplied to the SC results from the mixing of the primary flow with the recirculated secondary flow. The mass flow rates and flow temperatures at the outlet openings of the THS are inferred from mass and energy balances and can be deduced from Table 3 letting $\beta = 0$.

The thermal performance of the considered THSs is assessed in terms of the non-dimensional temperature ϑ, defined as

$$\vartheta \equiv \frac{T_1 - T}{\Delta T} \quad ; \quad \Delta T \equiv T_2 - T_3 \tag{1}$$

The deviation from the predictions of the base operation model can be ascribed to a *secondary* (*primary*) recirculation stream for $\gamma < 1$ ($\gamma > 1$). For $\gamma < 1$ the flow rate of the secondary bypass stream is $\gamma\,\beta\,\dot{m}$, while for $\gamma > 1$ the mass flow rate of the primary bypass stream is $\beta\,\dot{m}$, where $\dot{m}$ denotes the mass flow rate supplied from the PC. Invoking mass- and energy-conservation, while taking into account the flow distribution reported in Fig. 3, the non-dimensional temperatures of the different flow streams are derived under actual operation conditions (see Table 3). The non-dimensional temperature ϑ_2 provides a quantification of the off-design temperature drop occurring from the PC inlet (BIP) to the SC supply (PIP) and is directly related to the parameter β, as can be inferred from Table 3. Notice that the recirculated streams provide a simplified conceptualization of a more complex flow and energy distribution pattern within the device, which is affected by turbulent mixing, molecular diffusion and unsteadiness.

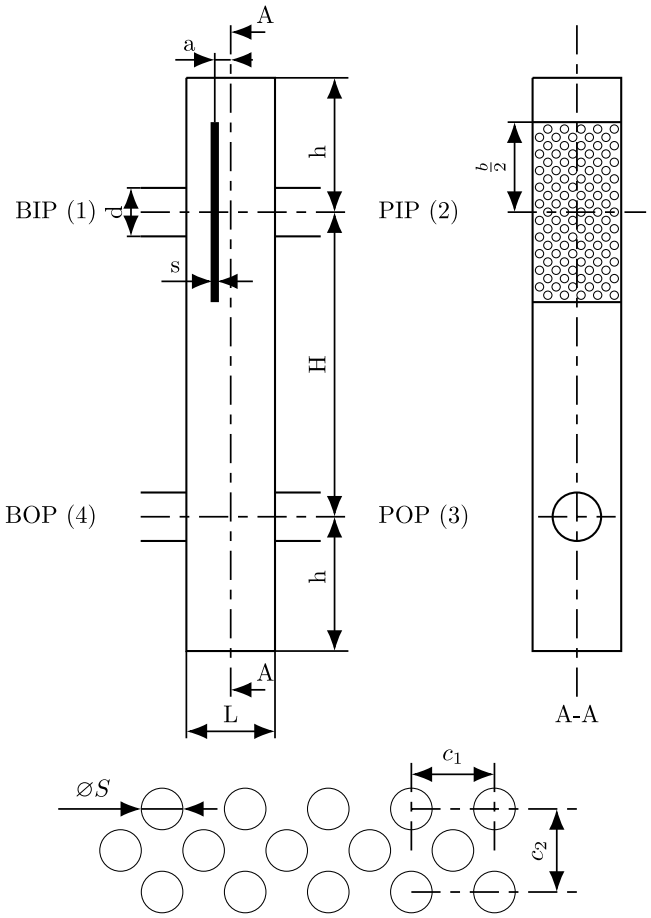

Fig. 1. Simplified representation of the considered THS and detail of the mesh strainer.

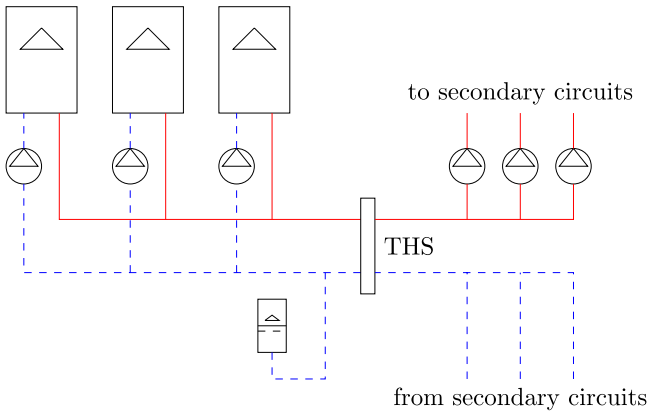

Fig. 2. Conceptual simplified scheme of a real-life application of a THS.

2.2. Fundamental modelling assumptions

The proposed model is based on the following assumptions:

- In most practical applications of the THS the working fluid is either water or a mixture of water/glycol while the case of the THS and the mesh strainer are made of stainless steel [5,10]. Both water and glycol can be modelled as incompressible Newtonian fluids [11, p. 279] while the stainless steel can be assumed as an incompressible and perfectly rigid material in the

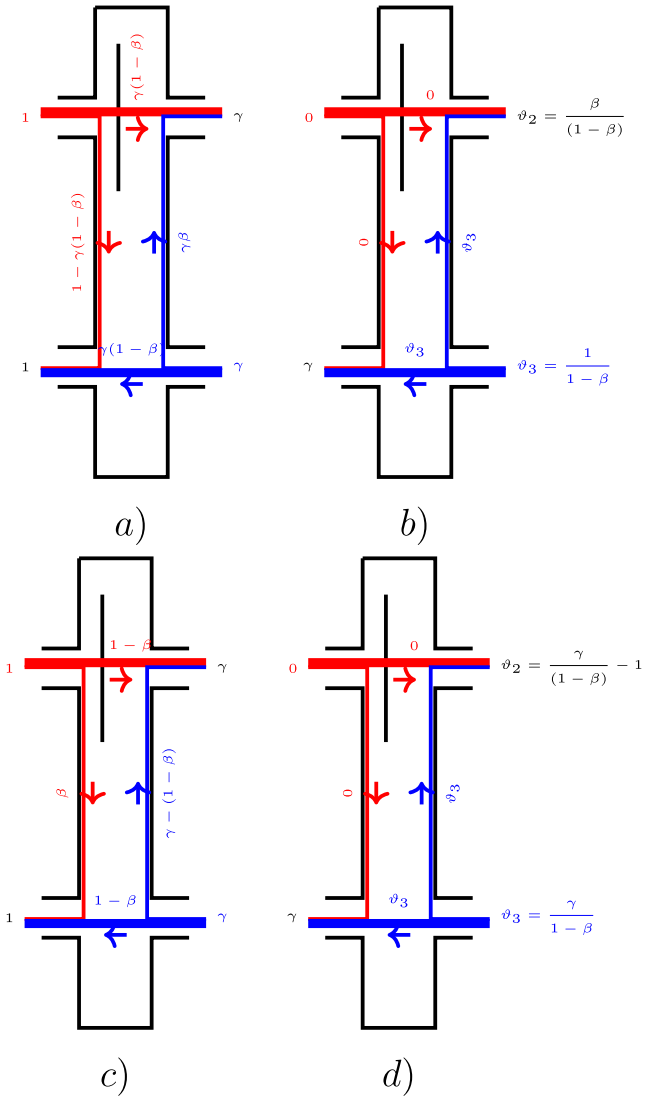

Fig. 3. Internal (left) flow and (right) temperature distribution. (a, (b) $\gamma \leq 1$, (c, (d) $\gamma > 1$.

considered range of pressure: the aforementioned assumptions have been accepted in the proposed physical model. The results are reported in dimensionless form, in order to extend their scope and to reduce the number of governing parameters: though this choice avoids the need of referring to specific materials, the considered values of the governing dimensionless groups result from selecting pure water and stainless steel as fluid and solid materials, respectively, and a range of fluid velocities common for practical applications of the THS.

- The relative volumetric expansion of the fluid is approximately 0.2% under a temperature change of 10 K, thus sufficiently modest to invoke the Boussinesq assumption [12].
- The viscous heating is neglected.
- As THSs are commonly used to distribute hot water from a heat generator to a heat dissipation network, values of the thermophysical properties of the materials at 65 °C have been chosen, considering a hypothetical yet realistic scenario where hot water is produced by a gas- or oil-fired boiler at 70 °C and a temperature drop of 10 °C takes place throughout the secondary circuit (see Table 4). The aforementioned thermophysical properties – except density – are assumed independent of temperature.
- In usual operation of THSs the flow-split ratio *gamma* is kept below 1.0. Nevertheless, under occasional off-design operation the secondary flow might exceed the primary flow: therefore, in the present investigation the flow split-ratio γ is varied within a range $[0, 2]$.

Table 4
Thermophysical properties of the materials, as derived from Lemmon et al. [13] (for water) and from Ulbrich Stainless Steels & Special Metals, Inc. [14] (for stainless steel UNS S30200).

Substance	ρ [kg/m^3]	c_p [J/kg K]	k [W/m K]	α_0 [K^{-1}]	μ [Pa s]
Water	980.55	4190.0	0.6553	5.52×10^{-4}	4.32×10^{-4}
Stainless steel	8030.0	502.0	16.27	0	– – –

2.3. Governing equations

The mass-, momentum- and energy-conservation equations for the fluid phase are:

$$\nabla \cdot \boldsymbol{u} = 0 \tag{2a}$$

$$\rho_0 \frac{\mathrm{D}\boldsymbol{u}}{\mathrm{D}t} = -\nabla P + \mu_0 \, \Delta \boldsymbol{u} - \rho_0 \, \alpha_0 \, \left(T - T_0\right) \, \boldsymbol{g} \tag{2b}$$

$$\rho_0 \, c_0 \, \frac{\mathrm{D}T}{\mathrm{D}t} = k_0 \, \Delta T \tag{2c}$$

The quantity P denotes the gauge pressure, i.e., the static pressure p reduced by the hydrostatic contribution:

$$P \equiv p - \rho_0 \, \boldsymbol{g} \cdot \boldsymbol{x} \tag{3}$$

The subscript 0 identifies the reference conditions, corresponding to standard atmospheric pressure and to a reference temperature T_0=298.15 K.

The mesh strainer is modelled as a three-dimensional solid, interested by heat conduction in its interior and exchanging heat with the surrounding fluid by convection. The energy conservation equation within the mesh strainer accounts only for the thermal diffusion:

$$\frac{\partial}{\partial t} \left(\rho_s \, c_s \, T\right) = \nabla \cdot \left[k_s \, \nabla T\right] \tag{4}$$

Both the temperature and the heat flux must be continuous at the fluid–solid interface:

$$T_f = T_s \tag{5}$$

$$-k_f \left.\frac{\partial T}{\partial n}\right|_f = -k_s \left.\frac{\partial T}{\partial n}\right|_s \tag{6}$$

The subscripts f and s denote the fluid and the solid sides of the interface, respectively, while $\boldsymbol{n}$ denotes the direction normal to the interface (with arbitrary orientation).

The physical quantities are made non-dimensional using the following *scales*: the diameter d of the connecting pipes, the mean inflow velocity U through the BIP, the temperature decay ΔT throughout the SC. Besides ϑ, the ensuing non-dimensional variables are formed:

$$\begin{aligned} \boldsymbol{x}^* &\equiv \frac{\boldsymbol{x}}{d} \qquad t^* \equiv \frac{t \, U}{d} \\ \boldsymbol{u}^* &\equiv \frac{\boldsymbol{u}}{U} \qquad \Pi^* \equiv \frac{P + \rho_0 \, \alpha_0 \, \boldsymbol{g} \cdot \boldsymbol{x} \, \left(T_1 - T_0\right)}{\rho_0 \, U^2} \end{aligned} \tag{7}$$

The non-dimensional governing equations for the fluid phase result from the mass- and from the momentum-conservation principles:

$$\nabla^* \cdot \boldsymbol{u}^* = 0 \tag{8a}$$

$$\frac{\mathrm{D}\boldsymbol{u}^*}{\mathrm{D}t^*} = -\nabla^* \Pi^* + \frac{1}{\mathrm{Re}} \, \Delta^* \boldsymbol{u} + \mathrm{Ri} \, \vartheta \, \frac{\boldsymbol{g}}{g} \tag{8b}$$

$$\frac{\mathrm{D}\vartheta}{\mathrm{D}t^*} = \frac{1}{\mathrm{Re} \, \mathrm{Pr}} \Delta^* \vartheta \tag{8c}$$

The energy conservation equation applicable within the mesh strainer can be cast as:

$$\frac{\partial \vartheta}{\partial t^*} = \frac{D_s}{D_f} \, \frac{1}{\mathrm{Re} \, \mathrm{Pr}} \, \Delta^* \vartheta \tag{9}$$

The governing Eqs. (8) and (9) are subjected to a set of boundary and initial conditions, reported in Table 5: they introduce the flow ratio γ and the ratio of thermal conductivities $k^* \equiv k_s / k_f$ as additional parameters.

The dimensionless groups Reynolds (Re), Richardson (Ri) and Prandtl (Pr) are defined using the properties of the working fluid at the reference conditions:

$$\mathrm{Re} \equiv \frac{\rho_0 \, U \, d}{\mu_0}; \quad \mathrm{Ri} \equiv \frac{g \, \alpha_0 \, \Delta T \, d}{U^2}; \quad \mathrm{Pr} \equiv \frac{\nu_0}{D_{f,0}} \tag{11}$$

Table 5
Boundary conditions for the governing equations.

Boundary	Type	Flow		Heat transfer	
External walls	No-slip, adiabatic	$\boldsymbol{u} = 0$		$\nabla T \cdot \boldsymbol{n} = 0$	
		$\boldsymbol{u}^* = 0$	(10a)	$\nabla^* \vartheta \cdot \boldsymbol{n} = 0$	(10b)
Strainer	Solid–fluid interface	$\boldsymbol{u} = 0$		$T_f = T_s,\ k_f \left.\frac{\partial T}{\partial n}\right\|_f = k_s \left.\frac{\partial T}{\partial n}\right\|_s$	
		$\boldsymbol{u}^* = 0$	(10c)	$\vartheta_f = \vartheta_s,\ \left.\frac{\partial \vartheta}{\partial n}\right\|_f = k^* \left.\frac{\partial \vartheta}{\partial n}\right\|_s$	(10d)
BIP	Mass-flow inlet	$\dot{m}_1 = \dot{m}$		T_1	
		$\dot{m}_1^* = 1$	(10e)	$\vartheta_1 = 0$	(10f)
PIP	Pressure outlet	$p_2 = 0$		$\nabla T \cdot \boldsymbol{n} = 0$	
		$\Pi_2^* = 0$	(10g)	$\nabla^* \vartheta \cdot \boldsymbol{n} = 0$	(10h)
POP	Mass-flow inlet	$\dot{m}_3 = \gamma\ \dot{m}$		$T_3 = T_2 - \Delta T$	
		$\dot{m}_3^* = \gamma$	(10i)	$\vartheta_3 = \vartheta_2 + 1$	(10j)
BOP	Mass-flow outlet	$\dot{m}_4 = \dot{m}$		$\nabla T \cdot \boldsymbol{n} = 0$	
		$\dot{m}_4^* = 1$	(10k)	$\nabla^* \vartheta \cdot \boldsymbol{n} = 0$	(10l)

The dimensionless pressure, velocity and temperature depend on position $\boldsymbol{x}^*$ and time t^*, on the Reynolds, Richardson and Prandtl numbers, on γ, D_s/D_f and k^*:

$$\boldsymbol{u}^*,\ \Pi^*,\ \vartheta = f\left(\boldsymbol{x}^*, t^*, \mathrm{Re}, \mathrm{Ri}, \mathrm{Pr}, \gamma, \frac{D_s}{D_f}, k^*\right) \tag{12}$$

where the thermal diffusivities of the solid and of the fluid are defined as

$$D_s \equiv \frac{k_s}{\rho_s c_s}; \quad D_f \equiv \frac{k_f}{\rho_f c_f}$$

Since a specific fluid (water) and a specific solid material for the mesh strainer (UNS S30200 stainless steel) are considered, some dimensionless groups are assumed constant:

$$\mathrm{Pr} = 2.79; \quad k^* = 24.83; \quad \frac{D_s}{D_f} = 25.15$$

As $\mathrm{Ri} \approx 0.05$ with the lowest considered inlet velocity, $U = 0.2\,\mathrm{m/s}$, the buoyancy forces are expected to be of minor relevance for the considered application. The product technical documentation usually limits the velocity U to less than $\sim 1\,\mathrm{m/s}$ (see, e.g., Caleffi [9],Caleffi JSC [10]), though lower velocities would further limit the turbulent mixing within the device.

2.4. Numerical model

The commercial CFD solver STAR-CCM$^+$ – 2021® by Siemens is used to solve the considered conjugate heat transfer problem. Turbulence is modelled by the Reynolds-Averaging approach [15], giving rise to unresolved turbulent stresses and heat fluxes, which are linked to the time-averaged flow quantities via the Realizable $k-\varepsilon$ turbulence model [15]. Further details about the used turbulence model are reported in Appendix A.

The mass, momentum and energy equations for the flow are solved simultaneously with a coupled flow solver with unsteady low-Mach preconditioning. The energy equation within the solid is advanced in time with an implicit scheme. The Roe-FDS scheme [16] with second-order upwind interpolation is used to approximate the inviscid fluxes. The calculation of the diffusive fluxes takes advantage of the so-called *secondary gradients* to reduce the errors related to the mesh skewness and non-orthogonality [17, Ch. 8]. The gradient of a transported quantity Φ at a cell centroid, $\nabla\Phi_0$, is calculated via a blending of the Gauss–Green and the least-squares methods. A limiter is applied to $\nabla\Phi_0$ when reconstructing the transported quantities on the centroids of the cell faces [18]. Heat is exchanged between fluid and solid through a conformal interface. The THS mounting the strainer is modelled by an unstructured mesh, obtained by a sequence of OcTree recursive subdivision (see, e.g., [19]), CutCell [20] and boundary inflation operations.

2.5. Validation of the numerical model

The proposed numerical model is validated by comparison with the experimental data by Yavorovsky et al. [3]. A THS with eight manifolds is connected to a heat source (electric boiler) and to either one or two heat consumers (a heat exchanger and a calorifer). The THS has a circular cross section with diameter $D = 41$ mm, height $H = 300$ mm, the internal diameter of the connected manifolds is $d = 11$ mm. The geometry of the considered device is shown in Fig. 4. The temperature inside the manifolds is measured with resistance thermometers under different operation conditions. In the present numerical model, the mass flow rates through the connected circuits are assigned, together with the supply temperature from the heating circuit and the return temperature from the heat consumer circuits. The numerical model is assessed by comparing the numerical and experimental predictions for the supply temperatures to all connected heat consumer systems. The numerical model exploits the Realizable $k-\varepsilon$ model with the two-layer near-wall correction strategy (further details are provided in Appendix A). An unstructured, polyhedral computational

Table 6
Some representative quality indicators for the computational mesh used for validating the proposed numerical model.

Metric		Min.	Max.	Ave.	St. dev.
Skewness angle	[°]	1.2×10^{-3}	86.9	17.0	15.1
Cell asp. ratio	[–]	0.168	1.0	0.955	0.0903
Cell vol. change	[–]	1.2×10^{-2}	1.0	0.79	0.27
Cell quality	[–]	2.6×10^{-3}	1.0	0.85	0.24
y^+ on case	[–]	0.028	73.01	5.86	7.17

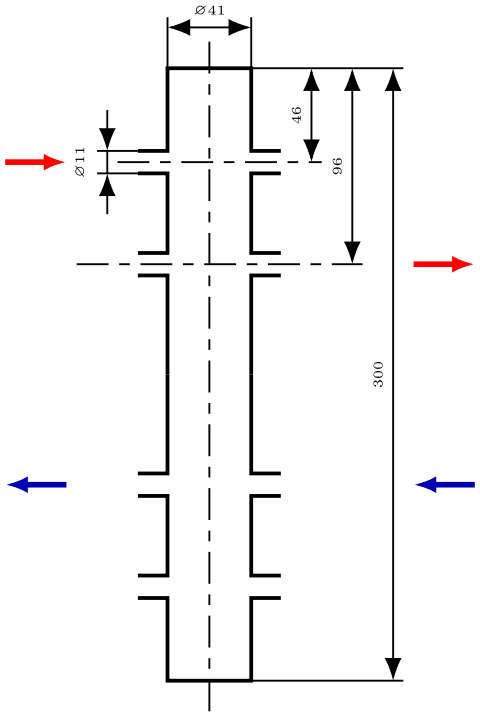

Fig. 4. THS investigated by Yavorovsky et al. [3]. Dimensions in mm.

mesh encompassing 844206 cells is used in the reported validation. Five layers of hexahedral cells cover the internal surface of the case of the THS. Some mesh-quality indicators are reported in Table 6.

The validation is carried out only for the case when a single consumer circuit is connected to the THS (the active connections are clearly identified in Fig. 4).

Table 7 compares the measured and simulated temperatures.

The percent discrepancy between the numerical and experimental outlet temperatures, relative to the difference between the inlet temperatures, does not exceed 1.67%, suggesting that the proposed numerical model is capable of representing the main features of the flow and temperature fields within a THS.

2.6. Sensitivity to the computational mesh

A block-structured computational mesh, formed only by hexahedral elements, is used to model the THS lacking of the strainer (same geometry shown in Fig. 1, with mesh strainer removed). Results obtained on six meshes with increasing number of cells have been compared in order to identify a reasonable compromise between accuracy and computational efficiency. For the considered test case, the inlet velocity through the BIP is 0.6 m/s and the flow split-ratio γ is 1.0. The percent relative errors (with respect to the finest considered mesh, encompassing $\gtrsim$ 900 000 cells) on the loss coefficients ξ_{tBB} and ξ_{tPP} pertaining respectively to the primary and secondary circuits and the non-dimensional temperature ϑ_2 are reported in Fig. 5. The mesh with 600 000 cells offers a reasonable compromise for both considered configurations of the THS and is used for the simulations.

Table 7
Comparison of the measured and simulated temperatures for the test case reported by Yavorovsky et al. [3] (one consumer circuit connected to THS).

Case		1	2	3	4
G_1 [m^3/h]		0.455	0.455	0.452	0.448
G_{ex} [m^3/h]		0.399	0.399	0.225	0.113
γ		0.877	0.877	0.498	0.252
T_1		50.21	48.65	48.38	49.69
T_2	Numerical	33.01	30.04	35.88	42.56
	Experimental	32.92	29.92	35.87	42.58
T_{ex1}	Numerical	49.98	48.38	48.37	49.68
	Experimental	50.1	48.53	48.17	49.21
T_{ex2}		30.38	27.14	23.29	21.56
ϑ_{ex1}	Numerical	0.0119	0.0128	0.0006	0.0002
	Experimental	0.00558	0.00561	0.000844	0.0174
ϑ_2	Numerical	0.878	0.8764	0.499	0.2536
	Experimental	0.877	0.87564	0.503	0.2608
$\frac{T_{ex1}^{exp} - T_{ex1}^{num}}{T_1 - T_{ex2}}$ [%]		−0.151	−0.697	+0.797	+1.670
$\frac{T_2^{exp} - T_2^{num}}{T_1 - T_{ex2}}$ [%]		+0.453	+0.557	+0.039	−0.035

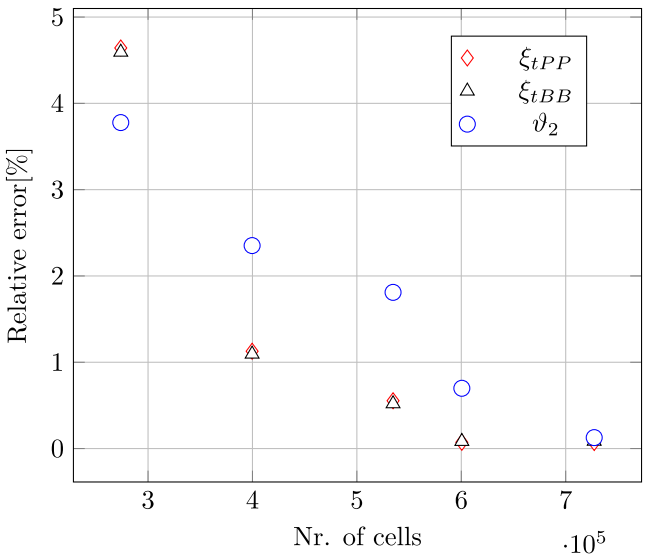

Fig. 5. Mesh sensitivity analysis for the THS without mesh strainer. The relative error is reported (in percent) for ξ_{tBB} (triangles), ξ_{tPP} (squares), ϑ_2 (circles).

3. Results

3.1. Flow and temperature pattern

The overall flow and temperature pattern within the THS, for different values of γ, can be inferred from Fig. 6. The local orientation of the flow field is represented via a line-integral-convolution (LIC) [21] (clearly discernible in the published electronic version of the article). A non-dimensional temperature $\widehat{\vartheta}$, ranging from 0 to 1, is the scalar associated with the LIC in Figs. 6:

$$\widehat{\vartheta} \equiv \frac{T - T_3}{T_1 - T_3} \tag{13}$$

The following evidence can be drawn:

- As for $\gamma < 1$, without the mesh strainer (Fig. 6(a)):
  - The recirculated primary flow moves downwards and prevents any significant temperature stratification: indeed, the central part of the barrel is almost entirely interested by the warm, recirculating primary flow.
  - The uppermost and the lowermost portions of the barrel, beyond the connecting pipes, are interested by recirculations of warm and cold fluid, respectively.

  - The return flow from the SC is *squeezed* towards the bottom of the barrel by the recirculating excess primary flow: this prevents any significant cooling of the primary flow supplied to the SC, consistently with the corresponding low value of ϑ_2 reported in Fig. 9.

- As for $\gamma < 1$, with the mesh strainer (Fig. 6(b)):
  - The mesh strainer deflects downwards the primary flow, so that the recirculating excess primary flow occupies must of the cross-section of the barrel's case. The downward flow prevents any significant entrainment in the PIP conduit of the cold fluid returning from the SC: indeed, ϑ_2 for $\gamma = 0.4$ is substantially unaffected by the presence of the mesh strainer and very close to 0 (see Fig. 9).

- As for $\gamma = 1.0$, without the mesh strainer (Fig. 6(c)):
  - Two equi-rotating recirculation regions develop in the central part of the barrel, as can be appreciated in Fig. 7: they entrain part of the warm and cold fluid supplied from the upper and lower jet streams, respectively, and convey it towards the centre of the barrel, where an intense temperature gradient builds up. The mixing of warm and cold fluid taking place in the centre of the barrel is consistent with the relatively large value of ϑ_2 for $\gamma = 1.0$ (see Fig. 9).

- As for $\gamma = 1.0$, with mesh strainer (Fig. 6(d)):
  - The blockage effect of the mesh strainer induces a downward diversion of the primary jet stream. Furthermore, by continuity, a layer of relatively cold fluid moves upwards and is entrained by the stream of fluid supplied to the SC. This evidence is consistent with the corresponding relatively large value of ϑ_2 (see Fig. 9).

- As for $\gamma > 1.0$ without the mesh strainer (Fig. 6(e)):
  - When the THS does not endow the mesh strainer, the flow and temperature pattern is qualitatively – as the Reynolds number of the flow through the BIP is higher – a mirrored representation of the case with flow split ratio $1/\gamma$, where the mirroring is applied both to the horizontal and to the vertical symmetry planes. This evidence is consistent with the expected minor importance of the buoyancy force, which is a source of vertical asymmetry.

- As for $\gamma > 1.0$ with the mesh strainer (Fig. 6(f)):
  - The mixing region between the warm primary stream and the recirculating secondary stream is wider than for the case without the mesh strainer. Nevertheless, the ascending flow is intense enough to prevent any mixing between the warm fluid (getting in through the BIP) and the fluid returning to the primary circuit (leaving through the BOP): therefore, the primary enthalpy flux is nearly entirely conveyed to the secondary circuit, consistently with the value of ϑ_2 being very close to the expectation from the *base* model for the THS (see Fig. 9).

3.2. Hydraulic separation

The head induced by the THS on the served circuits is quantified by a head-loss coefficient ξ_t, defined as

$$\xi_t \equiv \frac{2\,\Delta P_{\text{tot}}}{\rho\,U^2} \tag{14}$$

ΔP_{tot} is defined as the difference between the total pressure acting on the upper and the lower open sections of the device, located at a distance $1\,d$ from the barrel's case. Therefore,

$$\xi_{tPC} = \frac{2\left(P_{t,1} - P_{t,4}\right)}{\rho\,U^2}; \qquad \xi_{tSC} = \frac{2\left(P_{t,2} - P_{t,3}\right)}{\rho\,U^2} \tag{15}$$

The parameter ξ_t allows for a direct comparison of the THS with other common hydraulic components, e.g. valves. ξ_{tPC} and ξ_{tSC} refer to the head loss through the primary and through the secondary circuits, respectively. Fig. 8 shows the dependence of ξ_t on γ, where $0 \le \gamma \le 2$.

The solid and dashed lines represent the quadratic approximating polynomials for the THS mounting or lacking the mesh strainer, respectively. The corresponding data reported by Toneatti et al. [7] for a THS with circular cross section, not mounting a MTS, are reported for comparison. The head loss does not depend significantly on the shape of the cross section of the THS (either square or circular), in the range $0.5 \le \gamma \le 1.0$. Positive (negative) values of ξ_{tPC} imply that the THS contrasts (favours) the flow through the PC. Opposite considerations apply on the sign of ξ_{tSC}. Both ξ_{tPC} and ξ_{tSC} show a monotonically-decreasing dependence on γ.

The detrimental effect of the MTS on the hydraulic performance of the THS, though overall of modest significance, is more evident on ξ_{tSC}, which drops down to $\xi_{tSC} \approx -8$ when $\gamma = 2.0$: for comparison, the loss coefficient of a fully open globe valve is about 10. All in all, the MTS acts towards a decrease of the hydraulic efficiency of the THS. It causes an increase (reduction) in the magnitude of the pressure drop where it contrasts (favours) the flow throughout a connected circuit.

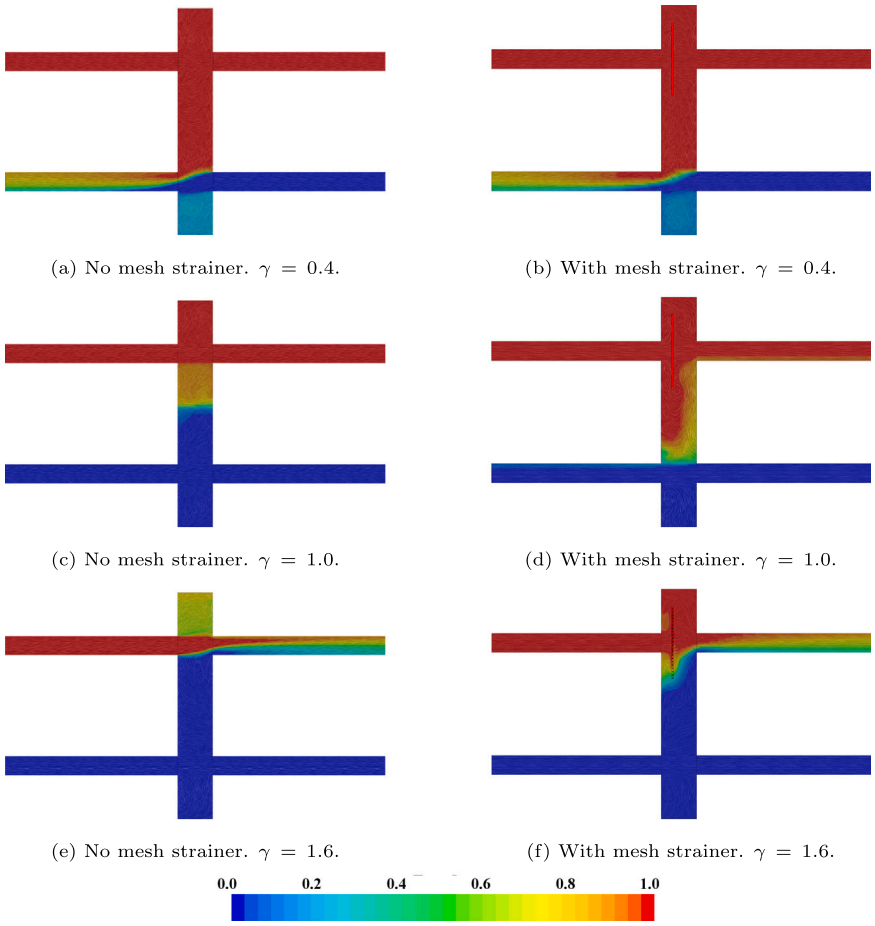

Fig. 6. Line-integral-convolution (LIC) representation of the flow field. Scaled temperature (13) is the scalar associated with the LIC.

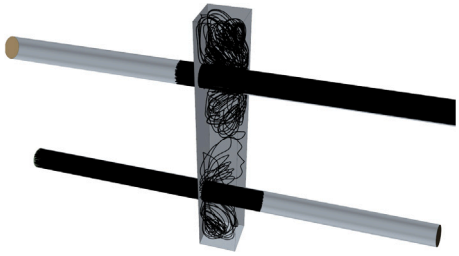

Fig. 7. THS without mesh strainer. $\gamma = 1.0$. Streamlines originating from within the BIP and POP inlet pipes.

3.3. Thermal dispatching

Fig. 9 shows the dependence of ϑ_2 on the flow split-ratio γ. The deviation from the expectations of the base operation model, represented as a solid line for $\gamma > 1$ (for $\gamma \leq 1$ the base operation model returns $\vartheta_2 = 0$), is comparatively larger for $\gamma \geq 1$ (though not evident in Fig. 9 due to the log-scale used on the vertical axis) and for the configuration of the THS mounting the mesh strainer. The maximum temperature deviation, occurring for $\gamma = 1$ with the MTS, is approximately 1.6% of ΔT. The trend reported by Toneatti et al. [7], for a THS with circular cross-section not mounting the MTS, though showing a relatively larger deviation from the *ideal* behaviour in the range $0.5 \leq \gamma \leq 1.0$, is consistent with the results reported here for the THS with square cross section.

The primary flow rate has been increased from 0.2 m/s up to 0.8 m/s to assess the dependence of the hydraulic and thermal parameters of the THS on it. The maximum suggested velocity of the primary flow for commercial THSs is about 1 m/s (see, e.g., Caleffi North America [22]). Table 8 reports values of ξ_{tPC}, ξ_{tSC} and ϑ_2 for the THS not mounting the MTS, for an assigned flow ratio $\gamma = 1.0$. Both ξ_{tPC} and ξ_{tSC} settle to a nearly constant value beyond $\mathrm{Re} \approx 33\,000$, while ϑ_2 settles for $\mathrm{Re} \geq 50\,000$. The

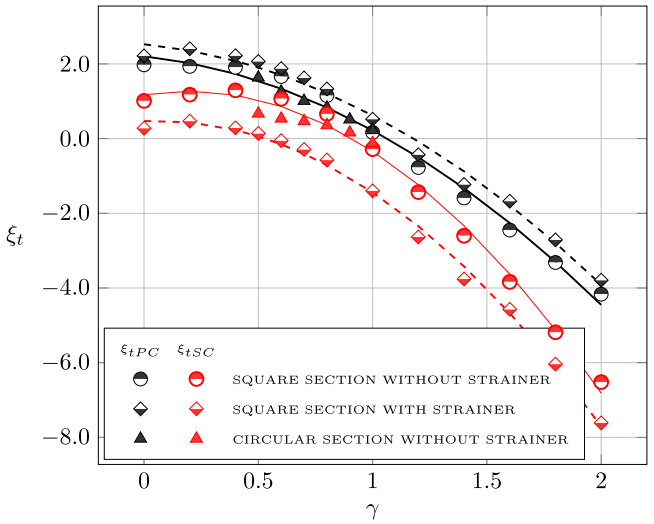

Fig. 8. Dependence of the head loss coefficient ξ_t on the flow ratio γ.

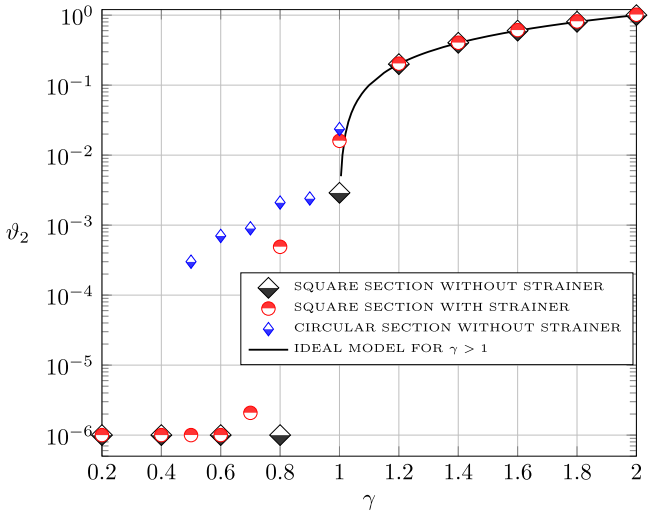

Fig. 9. Dependence of ϑ_2 on γ.

Table 8
Dependence of ξ_{tPC}, ξ_{tSC}, ϑ_2 on the Reynolds number of the primary flow for the THS without mesh strainer.

Re	U_{BIP}	ξ_{tPC}	ξ_{tSC}	ϑ_2
16671	0.213	0.167	−0.281	0.004
33280	0.425	0.197	−0.196	0.005
49919	0.637	0.196	−0.195	0.009
66559	0.849	0.199	−0.198	0.009

maximum temperature drop of the flow supplied to the SC is approximately 0.1 K when $\Delta T = 10$ K, for the highest considered Reynolds number.

3.4. Network models for the THS

Two block-model representations of the THS are proposed. The double-T node-and-branch representation of the THS (2T-THS) encompasses three independent hydraulic resistances and reproduces the actual hydraulic behaviour and the *ideal* thermal behaviour of the device, not accounting for the turbulent dispersion. Due to the moderate effect of turbulent dispersion on ϑ_2 under most

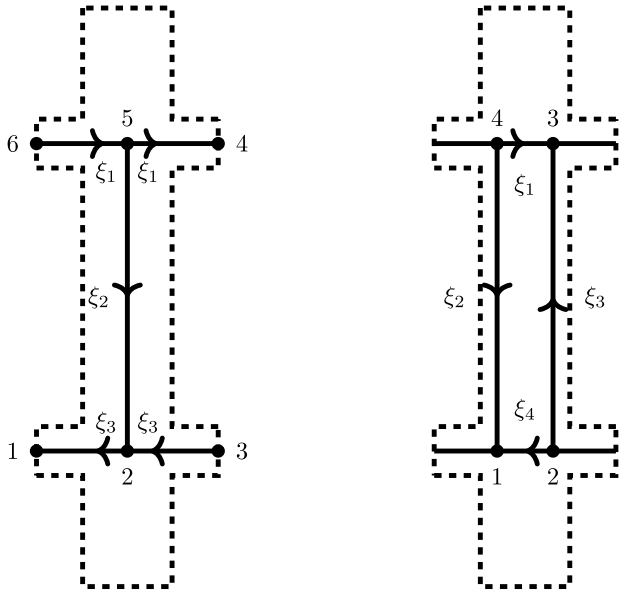

Fig. 10. Graph representation of (a) the 2T-THS model and (b) of the T4-THS model. The hydraulic resistance coefficients ξ are shown next to the associated branches.

operation conditions, the T2-THS model can be adequate for design purposes. The T4-THS model is made up of four hydraulic resistances: it improves the T2-THS model accounting for the effect of turbulent dispersion, thereby reproducing both the hydraulic and the thermal behaviour of the THS resulting from the numerical simulation.

Fig. 10(a) shows the graph structure of the 2T-THS model. The loss in the non-dimensional total pressure $\Delta\Pi^*$ through a branch, hereafter referred to as *head-loss* for brevity, is related to the flow rate along the same branch as

$$\Delta\Pi^* = \xi \frac{\dot{V}}{\dot{V}_{\mathrm{BIP}}} \tag{16}$$

The non-dimensional hydraulic resistance coefficient ξ depends on the split-ratio γ and on the Reynolds number Re (Eq. (11)): therefore, Eq. (16) conceals a non-linear dependence of $\Delta\Pi^*$ on $\dot{V}$. The coefficients ξ pertaining to all branches of the 2T-THS model are calculated by matching the values of $\widetilde{\Pi} \equiv \Pi^* - \Pi^*_{\mathrm{BIP}}$ at the PIP, POP and BOP sections:

$$\xi_1 = -\frac{\widetilde{\Pi}_{\mathrm{PIP}}}{1+\gamma} \tag{17a}$$

$$\xi_2 = \frac{\widetilde{\Pi}_{\mathrm{PIP}} - \widetilde{\Pi}_{\mathrm{POP}} - \widetilde{\Pi}_{\mathrm{BOP}}}{1-\gamma^2} \tag{17b}$$

$$\xi_3 = \frac{\widetilde{\Pi}_{\mathrm{POP}} - \widetilde{\Pi}_{\mathrm{BOP}}}{1+\gamma} \tag{17c}$$

Assuming that the heat transfer occurs by pure advection (i.e., $\beta = 0$), the 2T-THS model returns $\vartheta_2 = 0$ for $\gamma \leq 1$ and $\vartheta_2 = \gamma - 1$ for $\gamma > 1$.

Fig. 11 shows the dependence of ξ_1, ξ_2, ξ_3 on γ. Notice that ξ_1 and ξ_3 may become negative within certain ranges of γ, implying that the branches of the 2T-THS model act as non-linear *actuators* rather than behaving as gate-valves over the entire range of γ. Some features of the T2-THS model are prone to a physical interpretation, consistent with the outcomes of the three-dimensional CFD model:

- ξ_1 is significantly affected by the presence of the MTS. As for the THS not mounting the strainer, ξ_1 is negative in the range $0.2 \leq \gamma \leq 0.8$, suggesting that the upper branches (nodes $6-5-4$) act as a pump, transferring fluid from BIP to PIP. The hydraulic resistance coefficient ξ_1 for the THS with MTS is positive over the whole considered range of γ, as the strainer hampers the flow directed from BIP to PIP.
- ξ_3 is marginally affected by the presence of the MTS, as the mesh strainer does not extend beyond the upper half of the THS.
- ξ_1 and ξ_3 are remarkably different even for the THS not mounting the strainer. This feature results from the vertical asymmetry of the device. Indeed, whenever the upper *tee* acts as a flow splitter (mixer), the lower tee acts as a flow mixer (splitter). Furthermore, the off-centre location of the MTS contributes to the aforementioned asymmetry. It turns out that $\xi_1 \approx \xi_3$ for

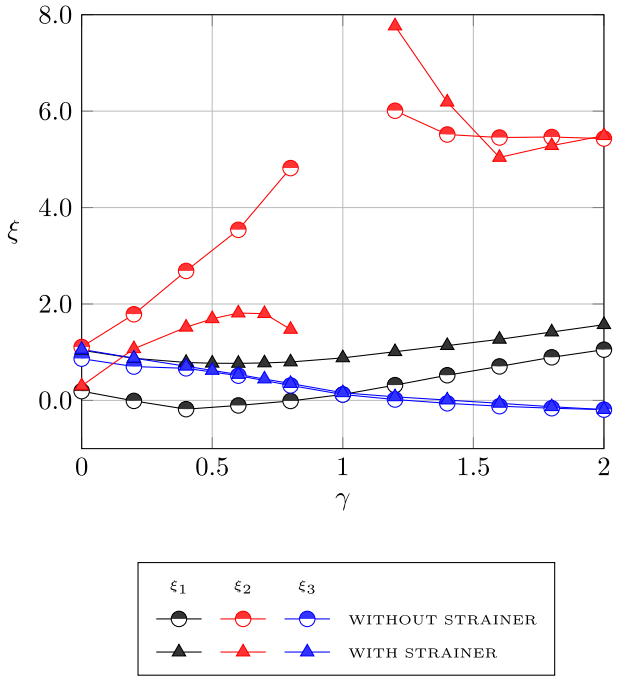

Fig. 11. T2-THS block model: dependence of ξ_1, ξ_2, ξ_3 on γ.

$\gamma = 1$ and only for the THS without mesh strainer, suggesting that buoyancy has only a minor impact on the aforementioned asymmetry.

- The resistance coefficient ξ_2 is either singular or indeterminate when $\gamma = 1$. Indeed, considering Fig. 10(a), it is evident that an infinite hydraulic resistance ξ_2 is required to prevent any appreciable flow through the corresponding branch, whenever $\Pi_5^* \neq \Pi_2^*$. Conversely, when $\Pi_5^* = \Pi_2^*$, no flow takes place through the central branch, irrespective of the value of ξ_2. In order to endow the T2-TSH in a more general network model, the value of ξ_2 should rise sharply for γ approaching 1, attaining a large, yet finite, positive value. For $\gamma < 1$, ξ_2 is significantly smaller for the THS mounting the strainer. This feature can be ascribed to the deflection of the flow induced by the strainer, which converts part of the x-momentum of the fluid into downward z-momentum and causes a positive (upward) vertical variation of the gauge pressure: Fig. 12 shows the steep decay of the dimensionless total pressure Π_t^* along a vertical line sample, taken within the THS mounting the strainer, with $\gamma = 0.5$. The line is contained in the symmetry plane of the device, at a distance of 6 mm from the strainer. For $1 < \gamma \leq 1.5$ the coefficient ξ_2 is higher for the THS mounting the strainer, suggesting that the strainer hampers the upward recirculation flow of the secondary circuit. For $\gamma > 1.5$ ξ_2 is only moderately affected by the presence of the MTS.

Fig. 10(b) shows the graph structure of the 4T-THS model. The hydraulic resistance coefficients are set according to the flow distribution shown in Fig. 3 and reported in Table 3 and to the values of the total gauge pressure at the connection ports of the THS, as calculated by the CFD model. Equations returning the calculated hydraulic resistance coefficients are reported in Appendix B.

The dependence of the four hydraulic resistance coefficients on γ is shown in Fig. 13. As expected, the strainer increases significantly the flow resistance ξ_1 in the upper branch, while ξ_4 is unaffected due to the limited vertical extension of the MTS.

Considering the configuration without MTS, the difference dependence on γ between ξ_1 and ξ_4 is due to their different interaction with the primary (for $\gamma < 1$) or with the secondary (for $\gamma > 1$) recirculated stream. For instance, referring to the case where $\gamma < 1$, the hydraulic resistance ξ_1 may be conceived as a series of a *local* resistance associated with a flow split (the recirculated primary flow is separated from the primary stream and diverted towards the BOP) followed by a hydraulic resistance encountered by the non-recirculated primary flow transferred from the BIP towards the PIP throughout the body of the THS. For the same value of γ, the hydraulic resistance ξ_4 may be conceived as a series of a hydraulic resistance opposing to the transfer of the returning secondary flow from POP to BOP, followed by a local resistance associated with the mixing of the recirculated primary flow with the secondary stream flowing from POP towards BOP. Notice that roughly corresponding flow conditions for ξ_1 and ξ_4 are obtained for values of γ and $2 - \gamma$ respectively, i.e.:

$$\xi_1(\gamma) \approx \xi_4(2 - \gamma) \tag{18}$$

The noteworthy decay of ξ_1 with increasing γ, for $\gamma < 1$ and for the configuration with the MTS, is conjectured to be caused by the onset of the bypass primary flow that circumvents the MTS to reach the PIP, instead of flowing through the perforated plate

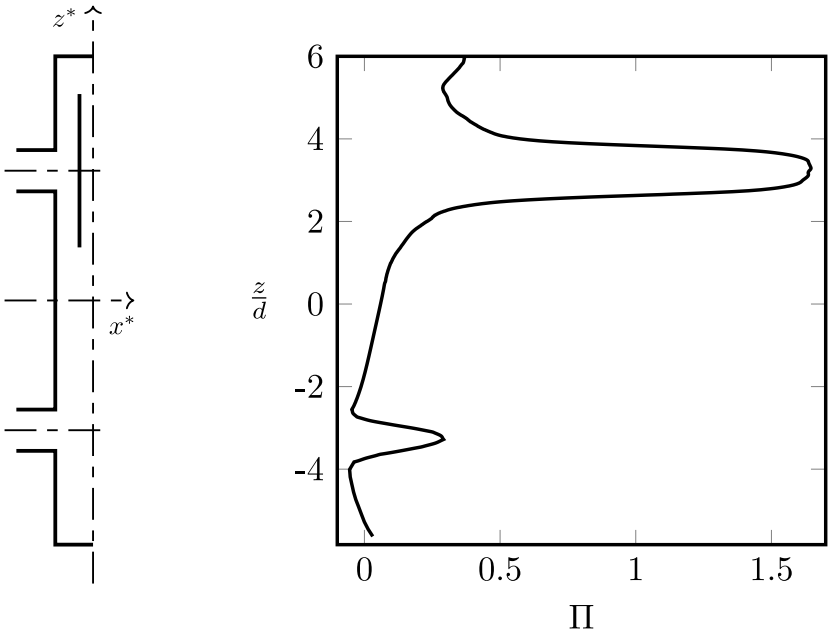

Fig. 12. Distribution of dimensionless total pressure Π_t^* along a vertical line: THS mounting the strainer, with $\gamma = 0.5$.

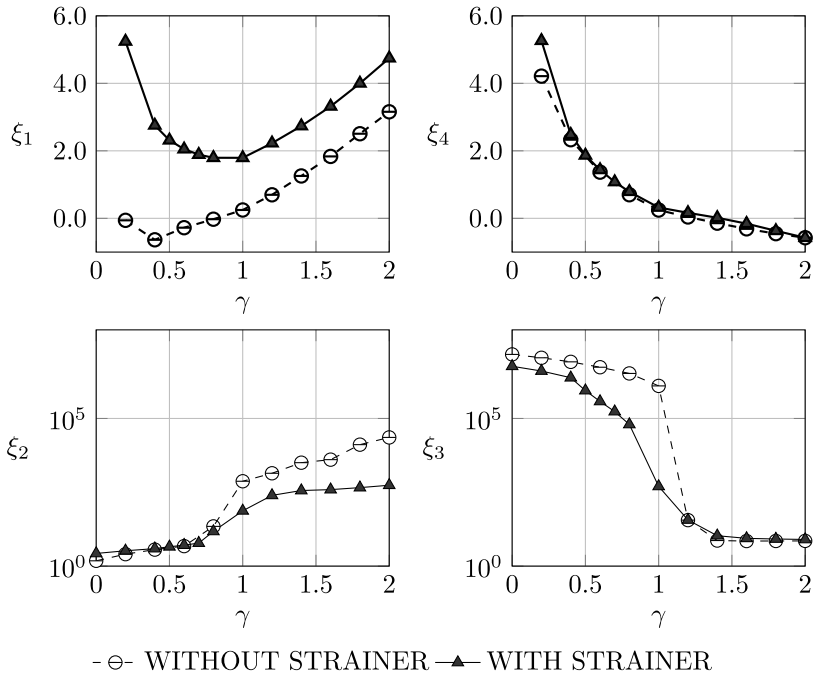

Fig. 13. T4-THS network model. Dependence of ξ_i on γ.

(see Fig. 6(b)). According to this conceptualization, the hydraulic resistance associated with the perforated plate, which contributed to ξ_1, becomes progressively less significant as γ increases towards 1.0.

For $\gamma < 1$ ($\gamma > 1$) the coefficient ξ_3 (ξ_2) attains very large positive (yet finite) values, as only a weak parasitic flow occurs through the corresponding branch.

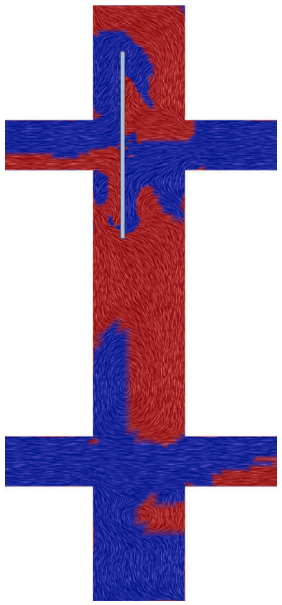

Fig. 14. Representations of the flow field on a cross-section of the THS. In red/blue colour: regions of downward/upward vertical velocity. (For interpretation of the references to colour in this figure legend, the reader is referred to the web version of this article.)

3.5. Unsteady operation of the THS

Once a thermal plant is activated or re-activated, it takes some time until it attains a stationary thermal condition. During this stage, the volume of the relatively cold water contained within the THS has to be washed out and the case of the THS has to be warmed up. We aim to assess the impact of the mesh strainer on the time the THS requires to attain stationary conditions. It is assumed that the flow field is already at a stationary condition. The mean velocity at the PC inlet section is $0.2\ \mathrm{m/s}$ and the flow split ratio is $\gamma = 1$. In the considered setup the case of the THS has a uniform initial temperature of 288.15 K (15 °C) and contains water at the same temperature. Water at 343.15 K (70 °C) and 333.15 K (60 °C) is supplied to the THS from the PC and SC, respectively. The fluid temperature rises gradually with time at the BIP and POP sections, since they are located at a distance of one diameter d from the main body of the THS and do not represent inlet boundaries for the computational model: steady values of the temperature (343.15 K and 333.15 K) are indeed assigned only at the aforementioned inlet boundaries. The reference time t_1 is defined as the time when the water temperature at the BIP attains 341.15 K (68 °C). The reference time t_2 is defined as the time when the water temperature at the PIP attains 342.65 K (69.5 °C). The reference time t_3 is defined as the time when the water temperature at the POP attains 331.15 K (58 °C). The reference time t_4 is defined as the time when the water temperature at the BOP attains 332.65 K (59.5 °C). The initial time t_0 of the warm-up stage is conventionally assumed as

$$t_0 = \frac{t_1 + t_2}{2}$$

The *warm-up time* Δt for the THS is defined as

$$\Delta t \equiv \max\left[\Delta t_2\,,\ \Delta t_4\right] \tag{19}$$

where

$$\Delta t_2 \equiv t_2 - t_0; \qquad \Delta t_4 \equiv t_4 - t_0 \tag{20}$$

Table 9 reports the warm-up times and other related times for the THS with and without the mesh strainer. The warm-up time Δt_4 is significantly shorter for the THS with mesh strainer, while Δt_2 is slightly larger. Fig. 14 shows a line integral convolution representation [23] of the flow pattern on a section plane of the THS+MS: the colour represents the distribution of the vertical velocity 7 seconds after t_0. The stream entering through the BIP is diverted by the strainer and must follow a longer path before reaching the PIP outlet. This explains the larger value of Δt_2 when the strainer is in place. Furthermore, the same blocking effect induces a faster descending stream of warm water from the BIP, which *penetrates* the volume of cold fluid stagnating in the core of the THS. This qualitative flow model provides a rationale for the lower value of Δt_4 for the THS+MS device.

4. Concluding remarks

Thermal–hydraulic separators are a widely used yet scantily investigated piece of hydraulic equipment. The scarcity of investigations concerning the hydraulic and thermal performance of THSs, in particular when endowed with a mesh strainer, as well

Table 9
Warm-up times for the THS with square cross-section.

Mesh strainer (Y/N)	Δt_2	Δt_4	Δt
Y	44.08	46.58	46.58
N	37.51	62.38	62.38

as concerning their internal flow and temperature pattern motivate the present study. This paper reports on a thorough numerical investigation of the thermal and hydraulic performances of a family of geometrically-similar thermal–hydraulic separators. The *standard* model for THSs, based on mass and energy balances, is improved to account for the turbulent mixing by introducing the concept of *parasitic streams*, whose intensity if represented by a single parameter β. A simple yet reliable network representation of the THS is derived therefrom.

The research highlights a remarkable efficiency of THSs both as hydraulic separators and as thermal dispatchers, under all the considered operating conditions: both the turbulent mixing and the presence of the mesh strainer impair marginally the performance of the considered THSs. The proposed block models support the physical intuition that represents the internal flow pattern as unmixed streams: the proposed model captures the effects of the turbulent mixing and could be integrated in thermal network solvers used for design and optimization.

Ensuing research could address the adaptability of the present work to THSs with an arbitrary number and arrangement of inflow/outflow ports. Though this investigation focuses on a THS with two inlet and two outlet connections, in principle the proposed characterization framework (in terms of internal currents) could be applied to THSs devices with a larger number of connections. To deal with such more complex configurations, a larger number of streams internal to the device must be considered, whose mass-flow rates should be determined by satisfying mass- and energy-conservation principles. Additional constraints must be devised to match the number of available equations with the number of unknowns.

CRediT authorship contribution statement

Marzio Piller: Conception and design of study, Acquisition of data, Analysis and/or interpretation of data, Writing – review & editing. **Luca Toneatti:** Acquisition of data, Analysis and/or interpretation of data, Writing – original draft, Writing – review & editing.

Declaration of competing interest

The authors declare that they have no known competing financial interests or personal relationships that could have appeared to influence the work reported in this paper.

Data availability

Data will be made available on request.

Acknowledgements

All authors approved the version of the manuscript to be published.

Funding

This research did not receive any specific grant from funding agencies in the public, commercial, or not-for-profit sectors.

Appendix A. Turbulence modelling

A.1. Realizable $k\epsilon$ model

The realizable $k-\varepsilon$ closure model (RKE) is used [24]. The rationale for this choice is that RKE is expected to provide improved predictions of the spreading rate of jets (it is known to resolve the so called *round-jet anomaly*) and of the most relevant features of flows involving rotation, compared to the standard $k-\varepsilon$ model (SKE): the flow streams ejected from the connection manifolds into the THS resemble round jets, which impact on the internal wall of the THS giving rise to regions of intense vorticity. The satisfactory validation of the proposed model against experimental data, reported in Appendix A, provides the conclusive argument supporting the use of the RKE model in the present investigation.

The components of the turbulent stress tensor derived within the RKE framework inherently satisfy the following *realizability* constraints:

Positivity:

$$\overline{u_k}\,\overline{u_k} \geq 0 \tag{A.1}$$

Cauchy-Schwartz inequality:

$$\frac{\overline{u_i}\,\overline{u_j}}{\overline{u_i^2}\,\overline{u_j^2}} \leq 1 \tag{A.2}$$

The RKE introduces a new formulation of the turbulent viscosity μ_t and some relevant modifications to the transport equation for the turbulent dissipation rate ε. The kinematic turbulent viscosity μ_t/ρ is still obtained from the product of a turbulent velocity scale $\sqrt{k}$ and a turbulent length scale $k^{3/2}/\varepsilon$ but, differently from the SKE model, the proportionality factor C_μ is not constant, as it depends on both strain and rotation [24]:

$$\mu_t = \rho\, C_\mu\, \frac{k^2}{\varepsilon} \tag{A.3a}$$

$$C_\mu = \frac{1}{A_0 + A_s\, U^* \dfrac{k}{\varepsilon}} \tag{A.3b}$$

The only adjustable parameter in Eq. (A.3b) is the constant A_0, where $A_0 = 4.0$ is used in the present study [24,25]. The strain-rate-related factor A_s is defined as [24]:

$$A_s = \sqrt{6}\cos\phi \tag{A.4a}$$

$$\phi = \frac{1}{3}\arccos\left(\sqrt{6}\,W\right) \tag{A.4b}$$

$$W = \frac{S^*_{ik}\,S^*_{kj}\,S^*_{ji}}{\left(\sqrt{S^*_{ij}\,S^*_{ij}}\right)^3} \tag{A.4c}$$

$$\boldsymbol{S}^* := \boldsymbol{S} - \frac{1}{3}\,S_{ii}\,\boldsymbol{I} \tag{A.4d}$$

where $\boldsymbol{S}$ denotes the rate of strain tensor.

The velocity scale U^* is related both to the strain-rate and to the rate of rotation of the fluid [24]:

$$U^* = \sqrt{S_{ij}\,S_{ij} + \Omega_{ij}\,\Omega_{ij}} \tag{A.5}$$

where $\boldsymbol{\Omega}$ denotes the mean vorticity tensor (in a non-rotating reference frame).

The RKE prescription (A.3b) returns values of C_μ that can occasionally deviate significantly from the constant value of 0.09, widely adopted in the SKE model. In this respect, Fig. A.15(a) shows the distribution of C_μ on a plane section of the considered THS with square cross-section ($U_{\text{in}} = 0.2$ m/s, $\gamma = 2.0$): C_μ takes values as large as 0.3 in regions of relatively low vorticity magnitude (Fig. A.15(b)).

The transport equation for the turbulent kinetic energy k is inherited from the SKE model, while the transport equation for the turbulent dissipation rate ε is obtained from a transport equation for the mean-square vorticity fluctuation $\overline{\omega_k\,\omega_k}$ (summation over k implied), recognizing that at large Reynolds number $\varepsilon \approx \nu\,\overline{\omega_k\,\omega_k}$ [26]:

$$\begin{aligned}\rho\frac{\mathrm{D}\varepsilon}{\mathrm{D}t} &= \frac{\partial}{\partial x_j}\left[\left(\mu + \frac{\mu_t}{\sigma_\varepsilon}\right)\frac{\partial\varepsilon}{\partial x_j}\right] + \underbrace{\rho\, C_{1\varepsilon}\, S\,\varepsilon}_{\text{Production}} \\ &- \underbrace{\rho\, C_{2\varepsilon}\,\frac{\varepsilon^2}{k+\sqrt{\nu\,\varepsilon}}}_{\text{Destruction}} + \underbrace{C_{1\varepsilon}\,\frac{\varepsilon}{k}\,C_{3\varepsilon}\,G_b}_{\text{Production by buoyancy}}\end{aligned} \tag{A.6}$$

Differently from the SKE, the production term of ε does not explicitly depend on the production term of k and the destruction term of ε is non-singular for k approaching zero. The model parameters are defined as follows:

$$C_{1\varepsilon} = \max\left(0.43\,;\,\frac{\eta}{5+\eta}\right);\quad \eta = \frac{S\,k}{\varepsilon}$$
$$C_{2\varepsilon} = 1.90;\quad \sigma_\varepsilon = 1.2$$

The buoyancy term is modelled according to the prescriptions by Henkes et al. [27]:

$$C_{3\varepsilon} = \tanh\left(\frac{v_b}{u_b}\right);\quad v_b = \left\|\overline{\boldsymbol{u}}\cdot\boldsymbol{g}\right\|\frac{\boldsymbol{g}}{g^2};\quad u_b = \left\|\overline{\boldsymbol{u}} - v_b\,\frac{\boldsymbol{g}}{g}\right\|$$

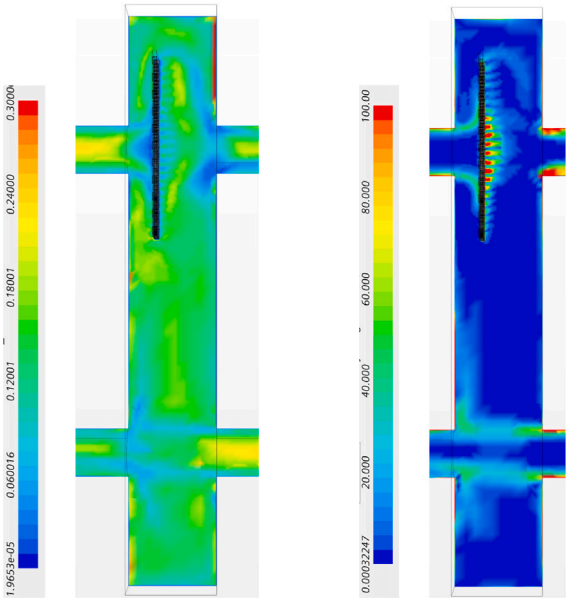

(a) C_μ calculated as in (A.3b).

(b) Vorticity magnitude.

Fig. A.15. Distribution of (a) C_μ and of (b) vorticity magnitude on a plane section of the considered THS with square cross-section.

A.2. Near-wall treatment

The shear-driven formulation [28] of a two-layer model [29] is adopted, where the turbulent dissipation rate and the turbulent viscosity are specified as functions of the wall distance in a layer near the wall. These functions are blended smoothly with the values computed from solving the transport equation for ε far from the wall. The equation for the turbulent kinetic energy is solved throughout the entire flow domain.

The two-layer near-wall model is used in combination with the all-y^+ wall function approach [25] in order to provide suitable wall boundary conditions for all the governing equations.

A stress boundary condition is enforced for the momentum equations, where the wall shear stress $\boldsymbol{t}_w$ is assigned as

$$\boldsymbol{t}_w = \rho u_\tau^2 \frac{\boldsymbol{v}_t}{\|\boldsymbol{v}_t\|_2} \tag{A.7}$$

with the velocity tangent to the wall given by

$$\boldsymbol{v}_t \equiv \boldsymbol{v} - \boldsymbol{v}\cdot\boldsymbol{n}\,\boldsymbol{n}$$

The friction velocity u_τ is calculated iteratively, by matching the scaled tangential velocity u_P^+ at the cell centroid P closest to the wall with the corresponding value provided by the blended wall function by Reichardt [30]:

$$u_P^+ = \frac{1}{\kappa}\log\left(1+y_P^+\right) + C\left[1 - \mathrm{e}^{-y_P^+/y_m^+} - \frac{y_P^+}{y_m^+}\mathrm{e}^{-b\,y_P^+}\right] \tag{A.8}$$

$$C = \frac{1}{\kappa}\log\left(\frac{E}{\kappa}\right) \tag{A.9}$$

$$b = \frac{1}{2}\left[y_m^+\frac{\kappa}{C} + \frac{1}{y_m^+}\right] \tag{A.10}$$

with

- $E = 9$ is assumed for the *log-law offset* coefficient,
- $\kappa = 0.42$ is taken for the von Karman constant,
- y_m^+ denotes the theoretical intersection point between the theoretical profiles for u^+ in the viscous and logarithmic layers ($y_m^+ \approx 10.92$).

The dimensionless temperature T^+ is defined as

$$T^+ \equiv \frac{T - T_w}{T^*} \tag{A.11}$$

where the *friction temperature* T^* is defined as

$$T^* \equiv \frac{q''_w}{\rho\, c_p\, u_\tau} \tag{A.12}$$

The *blended* wall function for T^+ is based on the wall function proposed by Jayatilleke [31] for the turbulent thermal boundary layer, matched with the theoretical temperature distribution within the conduction sublayer using the blending function proposed by Kader [32]:

$$T^+ = \mathrm{e}^{-\Gamma}\,\mathrm{Pr}\,y^+ + \mathrm{e}^{-1/\Gamma}\,\mathrm{Pr}_t\left[\frac{1}{\kappa}\log\left(E\,y^+\right) + P\right] \tag{A.13a}$$

$$\Gamma = \frac{0.01\,\left(\mathrm{Pr}\,y^+\right)^4}{1 + 5\,\mathrm{Pr}^3\,y^+} \tag{A.13b}$$

$$P = 9.24\left[\left(\frac{\mathrm{Pr}}{\mathrm{Pr}_t}\right)^{3/4} - 1\right]\left[1 + 0.28\,\exp\left(-0.007\,\frac{\mathrm{Pr}}{\mathrm{Pr}_t}\right)\right] \tag{A.13c}$$

Quoting Jayatilleke [31], *P is the resistance of the laminar sub-layer to heat transfer on account of the laminar Prandtl number of the fluid being different from* Pr_t. Specification of the wall heat flux provides the required boundary condition for the energy equation:

$$q''_w = \rho\, c_p\, u_\tau\,\frac{T_P - T_w}{T_P^+} \tag{A.14}$$

The non-dimensional, Reynolds-averaged cell temperature T_P^+ is given by the wall function (A.13).

A zero-flux wall boundary condition is enforced on the conservation equation for the turbulent kinetic energy:

$$\left.\frac{\partial k}{\partial n}\right|_w = 0 \tag{A.15}$$

Following the two-layer approach for modelling the near-wall turbulence, the dissipation rate of turbulent kinetic energy ε and the turbulent viscosity μ_t are assigned in the near-wall region [28,29]:

$$\varepsilon = \frac{k^{3/2}}{l_\varepsilon} \tag{A.16a}$$

$$l_\varepsilon = c_l\, d\,\left[1 - \exp\left(-\mathrm{Re}_d/(2\,c_l)\right)\right] \tag{A.16b}$$

$$c_l = 0.42\,C_\mu^{-3/4};\quad \mathrm{Re}_d = \frac{\sqrt{k}\,d}{\nu} \tag{A.16c}$$

$$\left(\mu_t\right)_{2L} = 0.42\,\mathrm{Re}_d\,C_\mu^{1/4}\left[1 - \exp\left(-\frac{\mathrm{Re}_d}{70}\right)\right] \tag{A.16d}$$

The turbulent viscosity (A.16d) is blended with the outer-flow solution, computed according to the Realizable $k-\varepsilon$ model (A.3):

$$\mu_t = \lambda\,\left(\mu_t\right)_{k\varepsilon} + (1-\lambda)\,\left(\mu_t\right)_{2L} \tag{A.17}$$

λ denotes the *wall-proximity indicator* as suggested by Jongen [33] (see also [25, Eq. (1155)]).

The conservation equation for ε is not solved down to the wall: rather, the value of ε at the centroid of a near-wall cell is assigned according to a universal law:

$$\varepsilon^+ \equiv \varepsilon\,\frac{\nu}{u_\tau^4} = \gamma\,\frac{2\,k^+}{(y^+)^2} + (1-\gamma)\,\frac{1}{\kappa\,y^+} \tag{A.18}$$

where the blending function γ is defined as

$$\gamma = \mathrm{e}^{-\mathrm{Re}_d/11} \tag{A.19}$$

Likewise, the production term in the conservation equation for k, is assigned in a near-wall cell according to a universal profile:

$$P_k^+ \equiv P_k\,\frac{\nu}{u_\tau^4} = \gamma\left[\frac{\mu_t}{\mu}\,\frac{\partial u^+}{\partial y^+}\right] + (1-\gamma)\,\frac{1}{\kappa\,y^+} \tag{A.20}$$

Appendix B. Hydraulic resistance coefficients for the T4-THS model

$$\xi_1 = \begin{cases} -\dfrac{\widetilde{\Pi}_{\mathrm{PIP}}}{\gamma\,(1-\beta)} & \gamma \le 1 \\ -\dfrac{\widetilde{\Pi}_{\mathrm{PIP}}}{1-\beta} & \gamma > 1 \end{cases} \tag{B.1a}$$

$$\xi_2 = \begin{cases} -\dfrac{\widetilde{\Pi}_{\mathrm{BOP}}}{1-\gamma\,(1-\beta)} & \gamma \le 1 \\ -\dfrac{\widetilde{\Pi}_{\mathrm{BOP}}}{\beta} & \gamma > 1 \end{cases} \tag{B.1b}$$

$$\xi_3 = \begin{cases} \dfrac{\widetilde{\Pi}_{\mathrm{POP}} - \widetilde{\Pi}_{\mathrm{PIP}}}{\gamma\,\beta} & \gamma \le 1 \\ \dfrac{\widetilde{\Pi}_{\mathrm{POP}} - \widetilde{\Pi}_{\mathrm{PIP}}}{\gamma-(1-\beta)} & \gamma > 1 \end{cases} \tag{B.1c}$$

$$\xi_4 = \begin{cases} \dfrac{\widetilde{\Pi}_{\mathrm{POP}} - \widetilde{\Pi}_{\mathrm{BOP}}}{\gamma\,(1-\beta)} & \gamma \le 1 \\ \dfrac{\widetilde{\Pi}_{\mathrm{POP}} - \widetilde{\Pi}_{\mathrm{BOP}}}{1-\beta} & \gamma > 1 \end{cases} \tag{B.1d}$$

References

[1] A. Yan, J. Zhao, Q. An, Y. Zhao, H. Li, Y.J. Huang, Hydraulic performance of a new district heating systems with distributed variable speed pumps, Appl. Energy 112 (2013) 876–885, http://dx.doi.org/10.1016/j.apenergy.2013.06.031.

[2] Y.V. Yavorovsky, Dmitry Romanov, V Sennikov, Ildar Sultanguzin, Alekcey Malenkov, E.V. Zhigulina, A Lulaev, Application of thermohydraulic dispatcher in low temperature district heating systems for decreasing heat carrier transportation energy cost and increasing reliability of heat supply, J. Phys. Conf. Ser. 891 (2017) 012167, http://dx.doi.org/10.1088/1742-6596/891/1/012167.

[3] Y.V. Yavorovsky, D.O. Romanov, V.G. Khromchenkov, Experimental research of thermo-hydraulic separators and dispatchers in heat supply systems, Solid State Phenom. 284 SSP (2018) 1385–1389, http://dx.doi.org/10.4028/www.scientific.net/SSP.284.1385.

[4] Elena Anisimova, Improvement of decentralized heat supply systems, IOP Conf. Ser.: Mater. Sci. Eng. 451 (2018) 012090, http://dx.doi.org/10.1088/1742-6596/451/1/012090.

[5] Mario Doninelli, Marco Doninelli, Claudio Ardizzoia, Idraulica, Caleffi, Inc., Fontaneto d'Agogna - 28010 - Novara (NO), ITALY, 2000.

[6] D.O. Romanov, Y.V. Yavorovsky, Investigation of thermohydraulic dispatcher properties and peculiarities, in: E3S Web of Conferences, Vol. 124, 2019.

[7] L. Toneatti, M. Piller, D. Pozzetto, E. Padoano, M. Boscolo, Hydraulic and thermal characterization of a family of thermo-hydraulic separators, Appl. Therm. Eng. (ISSN: 13594311) 179 (2020) http://dx.doi.org/10.1016/j.applthermaleng.2020.115701.

[8] K. Sotoodeh, Handling the pressure drop in strainers, Mar. Syst. Ocean Technol. 14 (4) (2019) 220–226, http://dx.doi.org/10.1007/s40868-019-00063-2.

[9] Caleffi, Idronics, Vol. 15, Caleffi North America, Inc., Milwaukee, Wisconsin, 2014, Retrieved from https://www.caleffi.com/sites/default/files/file/idronics_15_na_2019.pdf. (Accessed 06 July 2022).

[10] Caleffi JSC, Hydraulic separator n548 series, 2022, URL https://www.caleffi.com/sites/default/files/file/01076_en.pdf. Product technical document.

[11] A.V. Minakov, V. Ya Rudyak, M.I. Pryazhnikov, Rheological behavior of water and ethylene glycol based nanofluids containing oxide nanoparticles, Colloids Surf. A (ISSN: 0927-7757) 554 (2018) 279–285, http://dx.doi.org/10.1016/j.colsurfa.2018.06.051.

[12] P.K. Kundu, I.M. Cohen, D.R. Dowling, Fluid Mechanics, in: Science Direct e-books, Elsevier Science, ISBN: 9780123821003, 2012.

[13] Eric W. Lemmon, Ian H. Bell, Marcia L. Huber, Mark O. McLinden, in: P.J. Linstrom, W.G. Mallard (Eds.), NIST Chemistry WebBook, NIST Standard Reference Database Number 69, National Institute of Standards and Technology, Gaithersburg MD, 20899, 2022, http://dx.doi.org/10.18434/T4D303, Chapter Thermophysical Properties of Fluid Systems. (Accessed 5 July 2022) from.

[14] Ulbrich Stainless Steels & Special Metals, Inc., 302 Stainless Steel, UNS S30200, Ulbrich Stainless Steels & Special Metals, Inc., 153 Washington Avenue, North Haven, CT 06473 USA, 2022, from https://d2ykdomew87jzd.cloudfront.net/data-sheets/302-Stainless-Steel_Ulbrich-Revision-03-01-2016.pdf. (Accessed 5 July 2022).

[15] Stephen B. Pope, Turbulent Flows, Cambridge University Press, 2000, http://dx.doi.org/10.1017/CBO9780511840531.

[16] P.L. Roe, Characteristic based schemes for the Euler equations, Annu. Rev. Fluid Mech. 18 (1986) 337–365.

[17] F. Moukalled, L. Mangani, M. Darwish, The Finite Volume Method in Computational Fluid Dynamics: An Advanced Introduction with OpenFOAM and Matlab, first ed., Springer Publishing Company, Incorporated, ISBN: 3319168738, 2015.

[18] V. Venkatakrishnan, On the accuracy of limiters and convergence to steady state solutions, 1993, cited By 381.

[19] R. Schneiders, Octree-based hexahedral mesh generation, Int. J. of Comp. Geom. Appl. (2000).

[20] M. Berger, Chapter 1 - cut cells: Meshes and solvers, in: Rémi Abgrall, Chi-Wang Shu (Eds.), Handbook of Numerical Methods for Hyperbolic Problems, in: Handbook of Numerical Analysis, vol. 18, Elsevier, 2017, pp. 1–22, http://dx.doi.org/10.1016/bs.hna.2016.10.008, URL https://www.sciencedirect.com/science/article/pii/S1570865916300394.

[21] M. Han, H. Zhang, M. Bian, D. Zheng, Flow visualization based on enhanced streamline line integral convolution, Xitong Fangzhen Xuebao / J. Syst. Simul. 28 (12) (2016) 2933–2938, http://dx.doi.org/10.16182/j.issn1004731x.joss.201612008.

[22] Caleffi North America, SEP 4™ Combination Hydraulic, Air, Dirt and Magnetic Separator, Caleffi North America, 2021.

[23] B. He, K. Chen, Z. Yu, A LIC method for visualization of unstructured vector field, Jisuanji Yanjiu Yu Fazhan/Comput. Res. Dev. 43 (9) (2006) 1511–1515, http://dx.doi.org/10.1360/crad20060904.

[24] T.-H. Shih, W.W. Liou, A. Shabbir, Z. Yang, J. Zhu, A new $k-\varepsilon$ eddy viscosity model for high reynolds number turbulent flows, Comput. & Fluids 24 (3) (1995) 227–238, http://dx.doi.org/10.1016/0045-7930(94)00032-T.

[25] Siemens Digital Industries, STAR-CCM+ 15.06.007-R8 user's guide, 2021, URL https://www.plm.automation.siemens.com/global/en/products/simcenter/STAR-CCM.html.

[26] Henk Tennekes, John L. Lumley, A First Course in Turbulence, The MIT Press, ISBN: 9780262310901, 1972, http://dx.doi.org/10.7551/mitpress/3014.001.0001.

[27] R.A.W.M. Henkes, F.F. van der Flugt, C.J. Hoogendoorn, Natural convection in a square cavity calculated with low-Reynolds number turbulence models, Int. J. Heat Mass Transfer 34 (1991) 1543–1557.

[28] M. Wolfstein, The velocity and temperature distribution in one-dimensional flow with turbulence augmentation and pressure gradient, Int. J. Heat Mass Transfer 12 (1969) 301–318.

[29] W. Rodi, Experience with two-layer models combining the k-e model with a one-equation model near the wall, in: 29th Aerospace Sciences Meeting, AIAA, Reno, NV, 1991, AIAA-91-0216.
[30] H. Reichardt, Vollständige darstellung der turbulenten geschwindigkeitsverteilung in glatten leitungen, ZAMM - J. Appl. Math. Mech. / Z. Für Angew. Math. Und Mech. 31 (7) (1951) 208–219, http://dx.doi.org/10.1002/zamm.19510310704.
[31] C.L. Jayatilleke, The influence of Prandtl number and surface roughness on the resistance of the laminar sub-layer to momentum and heat transfer, Progress Heat Mass Transfer 1 (1969) 193–330.
[32] B.A. Kader, Temperature and concentration profiles in fully turbulent boundary layers, Int. J. Heat Mass Transfer 24 (1981) 1541–1544.
[33] T. Jongen, Simulation and Modeling of Turbulent Incompressible Flows (Ph.D. thesis), EPFL, Lausanne EPFL, 1998.